Assessment of Aortic Dissection Remodeling With Patient-Specific Fluid–Structure Interaction Models

Kathrin Bäumler, Malte Rolf-Pissarczyk, Richard Schussnig, Thomas-Peter Fries, Gabriel Mistelbauer, Martin R. Pfaller, Alison L. Marsden, Dominik Fleischmann, and Gerhard A. Holzapfel

***Abstract*—Aortic dissection leads to late complications due to chronic degeneration and dilatation of the false lumen. This study examines the interaction between hemodynamics and long-term remodeling of a patient's aortic dissection, tracked from pre-dissection to the chronic phase using CT angiography. Fluid–structure interaction models with tissue prestress, external support, and anisotropic properties were used to analyze hemodynamic markers. Each aortic wall layer had distinct thicknesses and material properties. The boundary conditions were guided by *in vitro* 4D-flow MRI and the patient's blood pressure. Aortic dilatation was most significant distal to the left subclavian artery, reaching 6 cm in the chronic phase. Simulations quantified the flow jet velocity through the entry tear, which peaked at 185 cm/s in the subacute phase and decreased to 123 to 133 cm/s in the chronic phase, corresponding to an increased entry tear size. Flow jet impingement on the false lumen resulted in a localized pressure increase of 11 and 2 mmHg in the subacute and chronic phases, with wall shear stress reaching 4 Pa. These hemodynamic changes appear to be the main drivers of aortic growth and morphological changes. Despite moderate overall flap movement, in-plane displacement increased from 0.6 to 1.8 mm as disease progressed, which was associated with an overall increase in aortic diameter. Simulations with a significant reduction in flap stiffness during the subacute phase resulted in increased flap motion up to 9.5 mm. Although these results are based on a single patient, they suggest a strong relationship between hemodynamics and aortic growth.**

***Index Terms*—Aortic dissection, remodeling, anisotropy, computational hemodynamics, fluid–structure interaction, patient-specific simulation, pre-dissection.**

Received 29 May 2024; revised 20 September 2024; accepted 9 October 2024. Date of publication 14 October 2024; date of current version 21 February 2025. The work of Malte Rolf-Pissarczy was supported in part by the Graz University of Technology, Austria, through the LEAD Project "Mechanics, Modeling, and Simulation of AD" (2018–2024) and in part by the Austrian Marshall Plan Foundation Scholarship 2022. The work of Martin R. Pfaller was supported in part by the NIH under Grant K99HL161313 and in part by the Stanford Maternal and Child Health Research Institute. The work of Alison L. Marsden was supported in part by the Stanford Research Computing Center through the computational infrastructure (Sherlock HPC cluster) and in part by the San Diego Super Computer Center. *(Kathrin Bäumler and Malte Rolf-Pissarczyk contributed equally to this work.) (Corresponding authors: Dominik Fleischmann; Gerhard A. Holzapfel.)*

Kathrin Bäumler and Gabriel Mistelbauer are with the 3D and Quantitative Imaging Laboratory, Department of Radiology, Stanford University, USA.

Malte Rolf-Pissarczyk is with the Institute of Biomechanics, Graz University of Technology, Austria.

Richard Schussnig is with the High-Performance Scientific Computing, University of Augsburg, Germany.

Thomas-Peter Fries is with the Institute of Structural Analysis, Graz University of Technology, Austria.

Martin R. Pfaller and Alison L. Marsden are with the Departments of Pediatrics and Bioengineering, Stanford University, USA.

Dominik Fleischmann is with the 3D and Quantitative Imaging Laboratory, Department of Radiology, Stanford University, Stanford, CA 94305 USA (e-mail: d.fleischmann@stanford.edu).

Gerhard A. Holzapfel is with the Institute of Biomechanics, Graz University of Technology, 8010 Graz, Austria, and also with the Department of Structural Engineering, Norwegian University of Science and Technology (NTNU), 7034 Trondheim, Norway (e-mail: holzapfel@tugraz.at).

This article has supplementary downloadable material available at https://doi.org/10.1109/TBME.2024.3480362, provided by the authors.

Digital Object Identifier 10.1109/TBME.2024.3480362

I. Introduction

PATIENTS who survive the acute phase of aortic dissection require lifelong monitoring of their dissected aorta. In contrast to the dramatic and life-threatening manifestation of an acute dissection, the chronic phase of aortic dissection has received comparatively little attention [1]. As more and more patients survive the acute phase [2], long-term management strategies such as lifelong surveillance imaging to monitor, prevent, and treat late adverse events become increasingly important. Late adverse events are primarily caused by degeneration of the false lumen (FL) wall and gradual aneurysmal dilatation. If the aortic diameter is more than 55 mm, surgical, endovascular, or hybrid interventions are recommended to reduce the risk of rupture [1]. Studies have examined the relationships between anatomical features and aortic growth, such as entry and exit tear sizes, initial aortic diameter, and false lumen thrombosis [3], [4]. However, the growth and remodeling of the FL vary widely among individual patients, and the mechanisms driving these changes remain poorly understood, hindering the development of personalized treatment strategies.

Hemodynamic factors such as false lumen pressurization are increasingly being investigated as predictors of late complications [5], [6]. To capture these metrics, advanced techniques such as time-resolved 3D phase-contrast magnetic resonance imaging (4D-flow MRI) [7] and computational fluid dynamics (CFD)

simulations are used. CFD models simulate virtual interventions, such as fenestration additions or occlusions, and evaluate the effects of endovascular treatments [8] and thrombus formation [9], [10], but their accuracy is limited by the assumption of rigid vessel walls.

Therefore, the development of fluid–structure interaction (FSI) models appears to be crucial to advance our understanding of the underlying mechanisms of this complex disease. There are few FSI studies on aortic dissections, primarily due to the substantial numerical challenge they pose [4]. In recent years, studies have validated FSI models using available *in vitro* or *in vivo* data [11], [12], compared their results to CFD simulations with rigid wall assumptions [13], studied false lumen pressurization with different tear sizes [12], or investigated the stress distribution and flap motion in cross-sectional studies [11], [14], [15]. Only a limited number of studies have also considered the microstructure of the aortic wall [14], [16].

Modeling the aortic wall is particularly interesting in aortic dissection because the dissection plane separates the histologic layers (intima, media, and adventitia) of the aorta into two functional layers with distinct microstructures and material properties: the inner layer consists mostly of elastic tissue, while the outer adventitial sleeve is mostly composed of non-compliant collagen.

In aortic dissection, the outer wall of the true lumen (TL) includes all aortic wall layers and generally resembles a normal aortic wall [17], though it may show medial degeneration [18]. The outer wall of the FL, mainly adventitia, is initially thin but thickens over time due to collagen deposition, exhibiting highly compliant mechanical behavior at low stretches but stiffening sharply at higher stretches. The dissection flap, made of delaminated elastic tissue, is highly mobile in the acute phase but stiffens as fibrosis progresses. To date, there is a lack of mechanical tests and microstructural investigations of these specific tissue layers that would allow a rigorous translation of mechanical experimental data into *in silico* models [4], primarily due to their laborious evaluation.

One aim of our study is to eliminate these deficits by increasing the physiologic relevance of the applied material models: we differentiate between functional tissue layers (outer wall of the TL, outer wall of the FL, and dissection flap) in the geometric 3D model according to layer-specific wall thickness values and by applying anisotropic material models with representative material parameters derived from layer-specific experiments on dissected tissue samples. These features have been added to our existing framework for FSI simulations of patient-specific aortic dissections with physiological boundary conditions, external tissue support, and prestress [11].

We aim to leverage our *in silico* model to investigate changes in hemodynamics and aortic growth in a patient with a medically treated type B aortic dissection. We followed the patient for seven years (and four computed tomography angiography (CTA) datasets), from the pre-dissection to the subacute and the chronic phase. At each time point, we examined FSI simulation results and anatomical changes, which provided us with the unique opportunity to qualitatively correlate growth-related hemodynamic markers and aortic growth over time. In this way, we aim to advance our understanding of the evolution and interplay of hemodynamics, biomechanics, and aortic remodeling that contributes to the most common late adverse event in aortic dissections, namely aortic dilatation.

II. Methodology

A. Patient, Imaging, and in vitro Data

We retrospectively selected four 3D CTA datasets from our institutional database from a female patient with Marfan syndrome who developed an acute type B aortic dissection at the age of 25. The research protocol was approved by the Stanford University Institutional Review Board (IRB-39377). The requirement for written consent was waived due to the retrospective nature of the study. Four imaging datasets were available; one pre-dissection ($\sim$24.5 months prior to onset) and three post-dissection in the subacute ($\sim$1.5 months after onset) and the chronic phase ($\sim$36 and $\sim$64 months after disease onset, respectively), see Fig. 1(a). Scan parameters and patient characteristics are detailed in Section I-B in the Supplementary Materials (Table S.I). During surveillance imaging, major aortic diameters were measured and represented in a 2D diameter plot [19], see Fig. 1(b).

At the time of disease onset, the patient was diagnosed with an acute, uncomplicated type B aortic dissection extending from just distal to the left subclavian artery (LSA) to just below the diaphragm in the distal thoracic aorta. The entry tear was located right after the LSA, while the exit tear was found superior to the celiac artery origin. Apart from small intercostal arteries, no other branch vessels emerged from the TL or FL. The patient received medical treatment and continuous monitoring using CTA imaging to monitor aortic growth and disease progression. During surveillance, the patient displayed a stable, chronic type B aortic dissection without evidence of acute dilatation or rupture. At no time was thrombosis observed. Measurements of the maximum aortic diameter showed a gradual but substantial increase compared to previous examinations (Fig. 1(b)). Eventually, the patient underwent open surgery to replace the descending aorta from the LSA to the supraceliac aorta with a Dacron graft. Although this post-repair diameter plot is included in Fig. 1(b), it was not included in this longitudinal computational study.

Patient-specific physiologic data were used to inform and tune simulation parameters and boundary conditions to closely resemble the patients physiology. We prescribed a pressure target of 125/75 mmHg for all four *in silico* studies. These blood pressure values were within 6% of the available patient-specific blood pressure cuff data at the first and third follow-up.

However, no *in vivo* information on flow rates and flow splits was available. We retrieved *in vitro* experimental data from a previous 4D-flow MRI phantom study [12]. In this study, a compliant 3D-printed model of the patient's subacute type B aortic dissection ($\mathcal{M}_1$) was created. The model was embedded in a flow and pressure-controlled setup consisting of an MRI-compatible flow circuit equipped with a programmable pump and capacitance and resistance elements to accurately replicate physiological conditions in terms of flow and pressure. This setup enabled direct measurement of flow rates and flow splits across all model boundaries. The corresponding dataset is available at the Stanford Data Repository (https://purl.stanford.edu/tz375fg1985).

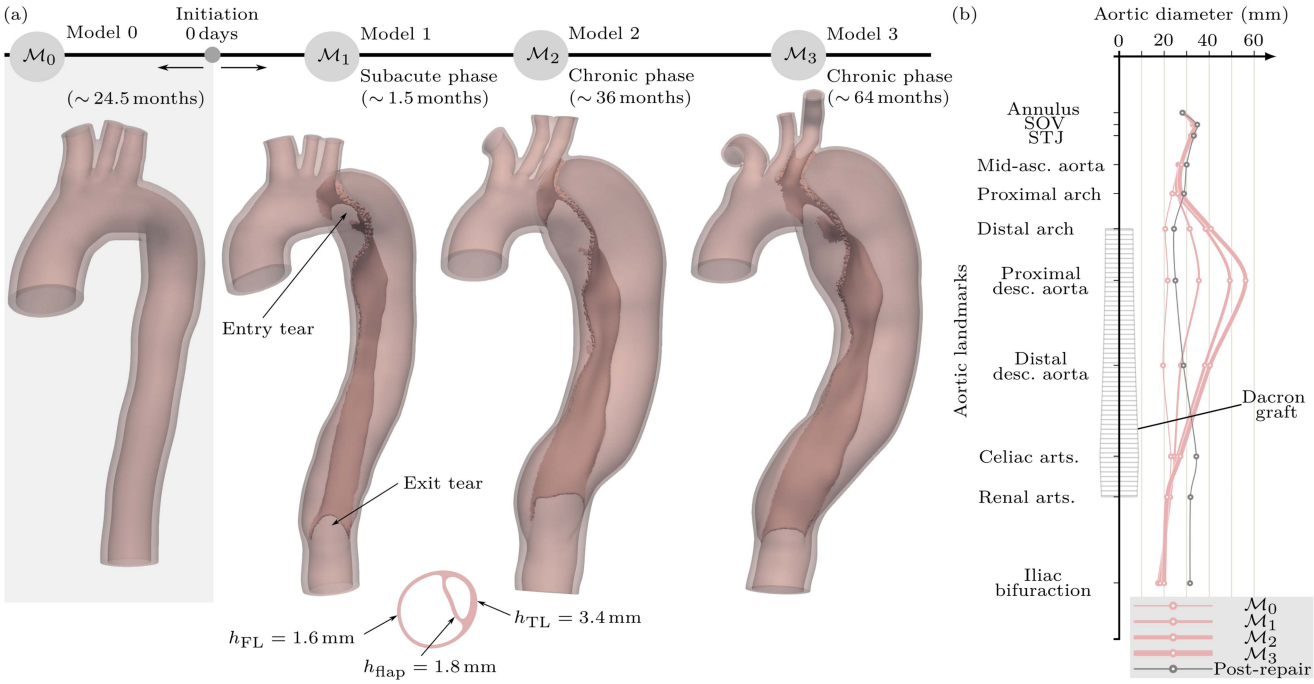

Fig. 1. (a) Reconstructed anatomical models from the pre-dissection CTA image ($\mathcal{M}_0$) and the three post-dissection follow-up CTA images: one in the subacute ($\mathcal{M}_1$) and two in the chronic phases ($\mathcal{M}_2$ and $\mathcal{M}_3$), where a timeline displays the chronological order of the CTA images. Exemplarily, the variations in wall thickness for $\mathcal{M}_1$ are illustrated in a representative cross-section. (b) Additionally, a diameter plot shows the evolution of the major diameter along the (straightened) aorta and the extent of the Dacron graft placed in the descending aorta post-$\mathcal{M}_3$ (SOV: sinus of Valsalva; STJ: sinotubular junction; asc.: ascending; desc.: descending; arts: arteries).

B. Model Generation

We segmented the patient-specific anatomical models from diastolic CTA images. These included one pre-dissection CTA image ($\mathcal{M}_0$) and three post-dissection follow-up CTA images: one from the subacute phase ($\mathcal{M}_1$) and two from the chronic phase ($\mathcal{M}_2$ and $\mathcal{M}_3$). The anatomical models included the brachiocephalic trunk (BCT), the left common carotid artery (LCA), and the LSA in the aortic arch. All other major arteries were distal to the dissected aorta and not within the segmented domain. Image segmentation and model generation was performed using SimVascular [20], an open-source software specifically designed for patient-specific cardiovascular flow modeling. Further refinement was performed using Meshmixer (Autodesk, Inc.), which allowed us to adjust the wall thickness of three distinct layers: the outer wall of the TL, the dissection flap, and the outer wall of the FL. The generated anatomical models are depicted in Fig. 1(a). Unstructured tetrahedral meshes were then generated in SimVascular using Tetgen [21]. This procedure yields the fluid and solid discretizations required for FSI simulation. The specific steps of this procedure are detailed are detailed in Section I-B in the Supplementary Materials.

The prescribed wall thickness values were based on existing literature [22] and unpublished *ex vivo* thickness measurements on aortic dissection tissue provided by S. Sherifova (Institute of Biomechanics, Graz University of Technology, Austria). These values were then adjusted based on clinical experience and the following requirements: (i) $h_{\mathrm{TL}} = h_{\mathrm{FL}} + h_{\mathrm{flap}}$ and (ii) a minimum tissue thickness of 1.6 mm. The wall thickness was then set to 3.4 mm for the outer wall of the TL (h_{TL}), 1.8 mm for the dissection flap (h_{flap}), 1.6 mm for the outer wall of the FL (h_{FL}), and 1.6 mm for the arch vessels including the BCT, the LCA, and the LSA (h_{branch}), see Fig. 1(a). The thickness values were applied to all dissected geometries, $\mathcal{M}_1$ to $\mathcal{M}_3$. For the case before dissection $\mathcal{M}_0$, we defined the wall thickness equal to the outer wall of the TL.

C. Governing Equations and Material Parameters

In these patient-specific models, we assumed that blood is an incompressible Newtonian fluid, a typical assumption for larger arteries [23]. The fluid flow is determined by the Navier-Stokes equations using the Arbitrary Lagrangian Eulerian (ALE) formulation, i.e.

$$\varrho_{\mathrm{f}}\hat{\partial}_t\mathbf{v} + \varrho_{\mathrm{f}}((\mathbf{v}-\hat{\mathbf{v}})\cdot\nabla)\mathbf{v} - \operatorname{div}\boldsymbol{\sigma}_{\mathrm{f}} = 0 \quad \text{in}\,\Omega_{\mathrm{f}}(t), \tag{1}$$

$$\operatorname{div}\mathbf{v} = 0 \quad \text{in}\,\Omega_{\mathrm{f}}(t), \tag{2}$$

taking into account the deformability of the fluid domain $\Omega_{\mathrm{f}}(t)$ through the grid velocity $\hat{\mathbf{v}}$ and the ALE time derivative $\hat{\partial}_t(\bullet)$.

The Cauchy stress tensor for the blood is symbolized by $\boldsymbol{\sigma}_{\mathrm{f}}$ and can be defined for a Newtonian fluid as $\boldsymbol{\sigma}_{\mathrm{f}} = \mu_{\mathrm{f}}(\nabla\mathbf{v} + \nabla\mathbf{v}^{\mathrm{T}}) - p\mathbf{I}$. Here, $\mathbf{v}$ represents the fluid velocity, and p signifies the pressure. The gradient operator ∇ refers to spatial derivatives in the Eulerian frame, while $\mathbf{I}$ stands for the identity tensor. The fluid density and viscosity are assigned constant values of $\varrho_{\mathrm{f}} = 1{,}060\ \mathrm{kg/m^3}$ and $\mu_{\mathrm{f}} = 4$ mPa s, respectively.

TABLE I
LAYER-SPECIFIC MATERIAL PARAMETERS ARE BASED ON [25], [26], [27], WITH μ, k_1, k_2, κ, AND ν DEFINED IN [24]

Tissue layer	μ (kPa)	k_1 (kPa)	k_2 (–)	κ (–)	ν (–)
Dissection flap	62.1	10.75	1.38	0.046	0.49
Outer wall of the FL	21.6	27.86	1.38	0.055	0.49
Outer wall of the TL	43.1	18.8	1.38	0.050	0.49

The aortic wall is modeled as a homogeneous, anisotropic, and nonlinear material. This is achieved by applying the Gasser-Holzapfel-Ogden (GHO) model [24] featuring two collagen fiber families embedded into a matrix material, wherein each family is distributed rotationally symmetrically with respect to its mean fiber direction across all three tissue layers. However, the material parameters are unique for each layer. To incorporate this into our framework, we introduce a mapping at time t that correlates a line element $\mathbf{X}$ from the reference configuration $\mathbf{\Omega}_{\mathrm{s}}^0$ to a line element $\mathbf{x}$ of the current configuration $\mathbf{\Omega}_{\mathrm{s}}$. This corresponds to the deformation gradient, which is defined as $\mathbf{F} = \mathbf{I} + \mathrm{Grad}_X \mathbf{u}$, where $\mathbf{u}$ denotes the displacement field of the solid. The balance of linear momentum can then be expressed by

$$\varrho_{\mathrm{s}} \partial_{tt} \mathbf{u} - \mathrm{Div}_X(\mathbf{FS}) = \mathbf{0} \quad \text{in} \quad \Omega_{\mathrm{s}}^0, \tag{3}$$

where $\varrho_{\mathrm{s}} = 1{,}200$ kg/m^3 represents the density of the solid and $\mathbf{S}$ stands for the second Piola–Kirchhoff stress tensor. External forces such as gravity have been neglected and the reference domain is independent of time t. The material parameters of the GHO model, specified in Table I, are based on experimental tests conducted on dissected tissue – specifically from layer-specific uniaxial extension tests of the media and adventitia [25] of a chronic dissection. We assume here that the material behavior of the dissection flap is equivalent to the material behavior of the media, and similarly, the material behavior of the outer wall of the FL is equivalent to the material behavior of the adventitial tissue. Finally, the outer wall of the TL is a homogeneous blend of both layers, proportionally weighted according to their thickness ratio. Moreover, due to the lack of phase-specific data, we applied identical material properties to all models. However, to account for the observed stiffening of the dissection flap over time, we performed additional simulations with reduced flap stiffness in the subacute phase ($\mathcal{M}_1$), see Section II-C in the Supplementary Materials.

The coupling of the fluid and solid domains at the fluid-solid interface $\Gamma(t)$ is governed by the kinematic and dynamic boundary conditions

$$\mathbf{v} = \partial_t \mathbf{u} \quad \text{on} \quad \Gamma(t), \tag{4}$$

$$\boldsymbol{\sigma}_{\mathrm{f}} \mathbf{n}_{\mathrm{f}} + \boldsymbol{\sigma}_{\mathrm{s}} \mathbf{n}_{\mathrm{s}} = \mathbf{0} \quad \text{on} \quad \Gamma(t). \tag{5}$$

Our numerical method resolves the interface conditions in a monolithic fashion, leveraging nodal correspondence of the fluid and solid meshes at the fluid–structure interface during model creation.

D. Prestress

The aortic wall is subject to continuous deformation by mechanical forces, primarily blood pressure. Given the stress exposure on the aorta during imaging, incorporating these conditions through prestressing the solid domain in FSI simulations is critical. We followed the method proposed by Hsu and Bazilevs [28] and determined a so-called prestress tensor $\mathbf{S}_0$, which leads to zero-displacements of the diastolic computational geometry under corresponding hemodynamic flow conditions. The prestress tensor was integrated by augmenting the stress tensor with $\mathbf{S}_0$, leading to the following result

$$\varrho_{\mathrm{s}} \partial_{tt} \mathbf{u} - \mathrm{Div}_X(\mathbf{F}(\mathbf{S} + \mathbf{S}_0)) = \mathbf{0} \quad \text{in} \quad \Omega_{\mathrm{s}}^0(t). \tag{6}$$

We note that the motion of the dissection flap, most notably during the acute phase of the condition, is likely guided by the existing pressure differences between the TL and the FL rather than the absolute blood pressure that the outer arterial wall experiences [11]. We therefore assumed that the dissection flap is not prestressed.

E. Boundary Conditions

At each ring-shaped outlet of the structural domain, we implemented homogeneous Dirichlet boundary conditions for the displacement $\mathbf{u} = \mathbf{0}$ to stabilize the outlets. Furthermore, the outer aortic wall is surrounded by various tissues and organs that limit its motion and expansion. To account for this, we included external tissue support through a Robin-type boundary condition, expressed as

$$\boldsymbol{\sigma}_{\mathrm{s}} \mathbf{n}_{\mathrm{s}} = -k_{\mathrm{s}} \mathbf{u} - c_{\mathrm{s}} \partial_t \mathbf{u} - p_0 \mathbf{n}_{\mathrm{s}}. \tag{7}$$

This approach is illustrated in Fig. 2(a) using a spring, a damper, and pressure to represent the forces involved and model the tethering of the outer aortic wall. This approach has been utilized in prior works to accommodate for viscoelastic effects related to tissue support on the outer aortic wall [11], [29], [30]. In the given equation, k_{s} and c_{s} represent parameters modeling the viscoelastic reaction of the external tissue, while p_0 denotes the external pressure in the thoracic and abdominal cavities. In agreement with a previous study [12], we specified non-zero values $k_{\mathrm{s}} = 1.8 \times 10^7$ N/m^3, $c_{\mathrm{s}} = 3.0 \times 10^4$ N s/m^3, and set $p_0 = 0$ Pa.

For the fluid domain, we prescribed a Dirichlet condition at the inlet (Fig. 2(a)), which was obtained from previous *in vitro* experiments using 2D phase-contrast MRI [12]. At the four outlets we implemented three-element Windkessel boundary conditions to incorporate resistance and compliance effects of the downstream vasculature [31]. The Windkessel parameters required model-specific tuning to approximate the prescribed physiologic pressure targets and flow splits. Details on the tuning process and parameters can be found in Section I-C in the Supplementary Materials.

While material model parameters, external tissue support parameters, pressure targets, inflow waveform, and flow splits were prescribed identically for all models, we adjusted the the Windkessel parameters to achieve the prescribed pressure. Tuning was considered successful if the systolic blood pressure

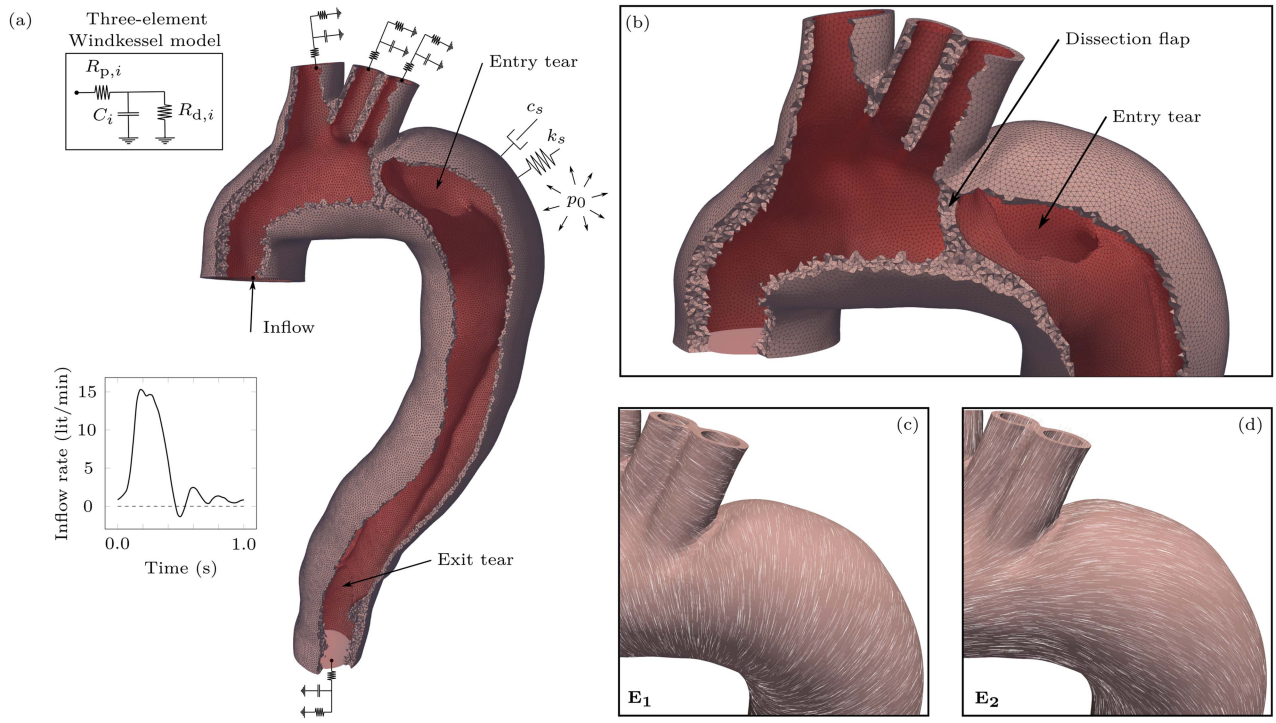

Fig. 2. Discretization of a representative anatomical model ($\mathcal{M}_1$) using finite elements, the prescribed inlet flow rate, the three-element Windkessel models at the four flow outlets, and the Robin-type boundary condition (7) on the outer aortic wall (a). Detailed view of a section of the solid mesh (b) and the local coordinate system for this anatomical model: circumferential direction $\mathbf{E}_1$ (c) and axial direction $\mathbf{E}_2$ (d).

P_{sys}, the diastolic blood pressure P_{dia}, the mean blood pressure $P_{\mathrm{mean}} = 1/3(P_{\mathrm{sys}} + 2P_{\mathrm{dia}})$ and the pressure amplitude (or pulse pressure) $P_{\mathrm{P}} = P_{\mathrm{sys}} - P_{\mathrm{dia}}$ aligned within a 10% tolerance of the pressure target (125/75 mmHg). Tuning parameters and their accuracy can be found in the Supplementary Materials (Tables S.II and S.III).

F. Local Coordinate System

The use of anisotropic material models required the definition of mean fiber directions in each cell of the solid domain. These in turn relied on physiologically meaningful local material orientations, or a local coordinate system. For complex patient-specific geometries, such as those encountered in aortic dissection, this poses a substantial challenge. Typically, the methods employed involve solving several Laplace problems in sequence to first compute the axial direction $\mathbf{E}_2$, followed by a subsequent step to determine the circumferential direction $\mathbf{E}_1$; both directions act in the reference frame.

However, as described in [16], we replaced the second Laplace problem for the circumferential direction with a more versatile algorithm, targeted towards an application in aortic dissections: the average normal vector on the fluid–structure interface was extrapolated into the structural domain, thereby approximating the normal direction of the tissue to obtain the radial direction $\mathbf{E}_3$. The mean orientations of all elements of the dissection flap were then determined by averaging over the thickness of the wall. Finally, the missing circumferential direction was derived from the cross product of the other two vectors. The resulting circumferential and axial directions are shown for $\mathcal{M}_1$ in Figs. 2(c) and (d). The local coordinate system was then utilized to determine the mean fiber direction for each of the two symmetrically aligned fiber families.

G. Discretization and Numerical Solver

To determine the required spatial resolution, we executed a series of simulations on increasingly refined meshes with uniform edge sizes of 1.0, 0.8, and 0.6 mm for the pre-dissection geometry. It was observed that a resolution of 0.8 mm provided satisfactory agreement with the finest mesh, whilst keeping the computational expense at an acceptable level. The number of tetrahedral elements for the final meshes is given in the Supplementary Materials (Table S.IV).

The numerical simulations were performed using the open-source finite element solver svFSI [20], [32], as provided by SimVascular. svFSI has a generalized second-order α time-stepping scheme and uses linear tetrahedral elements for pressure and velocity, incorporating pressure and momentum stabilization through a variational multiscale approach. This also includes the monolithic coupling of the fluid and structural domains, the preconditioning of the resulting linear systems and the backflow stabilization at the fluid outlets [33], [34]. We employed an iterative GMRES linear solver together with a resistance preconditioner as detailed in the related literature [34], [35]. The temporal resolution was set to 4,000 time steps per cardiac cycle (duration $T = 1.0$ s) leading to a time step size of 0.25 ms.

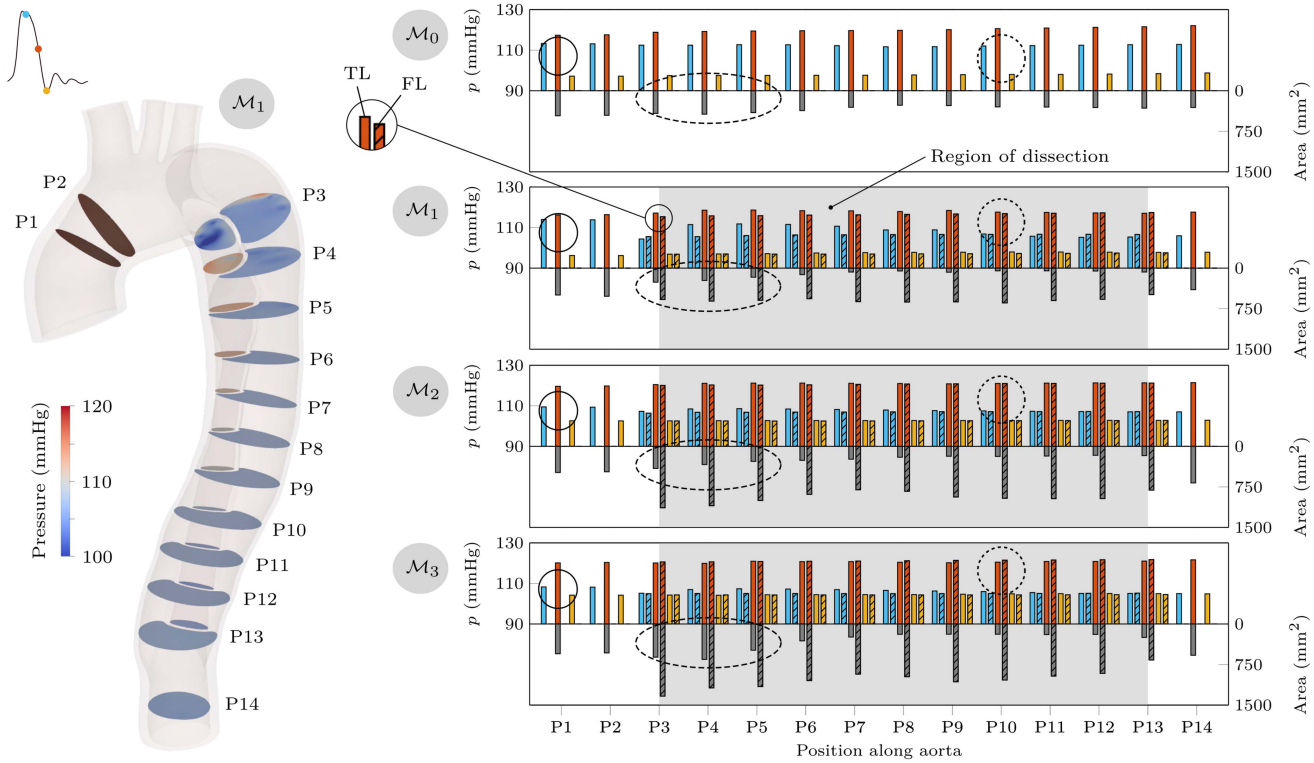

Fig. 3. The pressure distribution in the TL and FL at the 14 positions is shown for a representative model ($\mathcal{M}_1$). The absolute pressure p (colored bars; left scale) and lumen area (gray bars; right scale) of TL and FL are displayed at 14 positions for all models along the aorta (P1 to P14; hatched bars for FL), where the data are presented for three cardiac phases (peak systole: cyan, mid-deceleration systole: orange, and end systole: yellow; see top left scale) and one representative phase (mid-deceleration systole: gray), respectively. The gray overlay highlights the dissection region.

For the FSI simulations we utilized the Expanse HPC system of the San Diego Supercomputer Center (SDCC) and requested between 1 and 3 AMD EPYC 7742 compute nodes with 128 cores each. The duration for the simulation of a full cycle varied between approximately three to four hours, depending on the respective mesh size and number of nodes used.

We simulated at least seven cardiac cycles to ensure cycle-to-cycle periodicity of the simulation results [36]. Cycle-to-cycle periodicity was evaluated by comparing pressure results from subsequent cycles (P_{sys}, P_{dia}, P_{mean}, and P_{P}). Periodicity was considered achieved when the cycle variation was less than 0.5%. Simulations of the final cardiac cycle were then written to 'Visualization Toolkit' (VTK) unstructured grid files with cardiac cycle time steps of 80, resulting in a time frame length of 12.5 ms.

III. Results

A. Anatomical Remodeling

Clinical surveillance measurements revealed an increase in the maximum aortic diameter from pre-dissection (22 mm) to 35, 49, and 56 mm in models $\mathcal{M}_1$, $\mathcal{M}_2$, and $\mathcal{M}_3$, respectively. The largest diameter was consistently found at the proximal descending aorta, as shown in Fig. 1(b). The TL volume, measured from the entry to the exit tear, almost tripled over the course of the disease with 18, 35, and 52 ml in $\mathcal{M}_1$, $\mathcal{M}_2$, and $\mathcal{M}_3$. Likewise, the FL volume doubled with 111, 183, and 227 ml in $\mathcal{M}_1$, $\mathcal{M}_2$, and $\mathcal{M}_3$. During aortic remodeling, not only did the aortic diameter and volume increase, but the remodeling also varied along the dissection. To quantify this, the aortic tapering ratio R_{TAP} was calculated by comparing the proximal and distal cross-sectional areas (P3 and P13; Fig. 3). Pre-dissection, the aorta exhibited a slight taper ($R_{\text{TAP}} = 1.3$). The taper sharply increased for the TL in the subacute phase ($\mathcal{M}_1$) and decreased subsequently during the chronic phase. In contrast, FL showed the lowest tapering ratio at $\mathcal{M}_1$ but continued to increased with disease progression (Table II).

TABLE II
Cross-Sectional Areas in mm^2 at P3 and P13 (Fig. 3). R_{TAP} Quantifies the Tapering Along the Proximal Descending Aorta

	$\mathcal{M}_0$		$\mathcal{M}_1$	$\mathcal{M}_2$	$\mathcal{M}_3$
A_3	397.2	$A_{\text{TL},3}$	247.2	396.5	600.7
		$A_{\text{TL},13}$	72.5	168.2	245.8
A_{13}	301.0	$A_{\text{FL},3}$	561.2	1,098.0	1,290.1
		$A_{\text{FL},13}$	459.8	770.3	629.6
R_{TAP}	1.3	$R_{\text{TAP,TL}}$	3.4	2.4	2.4
		$R_{\text{TAP,FL}}$	1.2	1.4	2.1

To assess the diastolic tear areas, we identified a ring of surface elements around each tear. The curved surface areas measured were 336, 802, and 427 mm^2 in $\mathcal{M}_1$, $\mathcal{M}_2$, and $\mathcal{M}_3$, respectively, while the exit tear area measurements were in 377, 738, and 303 mm^2 in $\mathcal{M}_1$, $\mathcal{M}_2$, and $\mathcal{M}_3$, respectively.

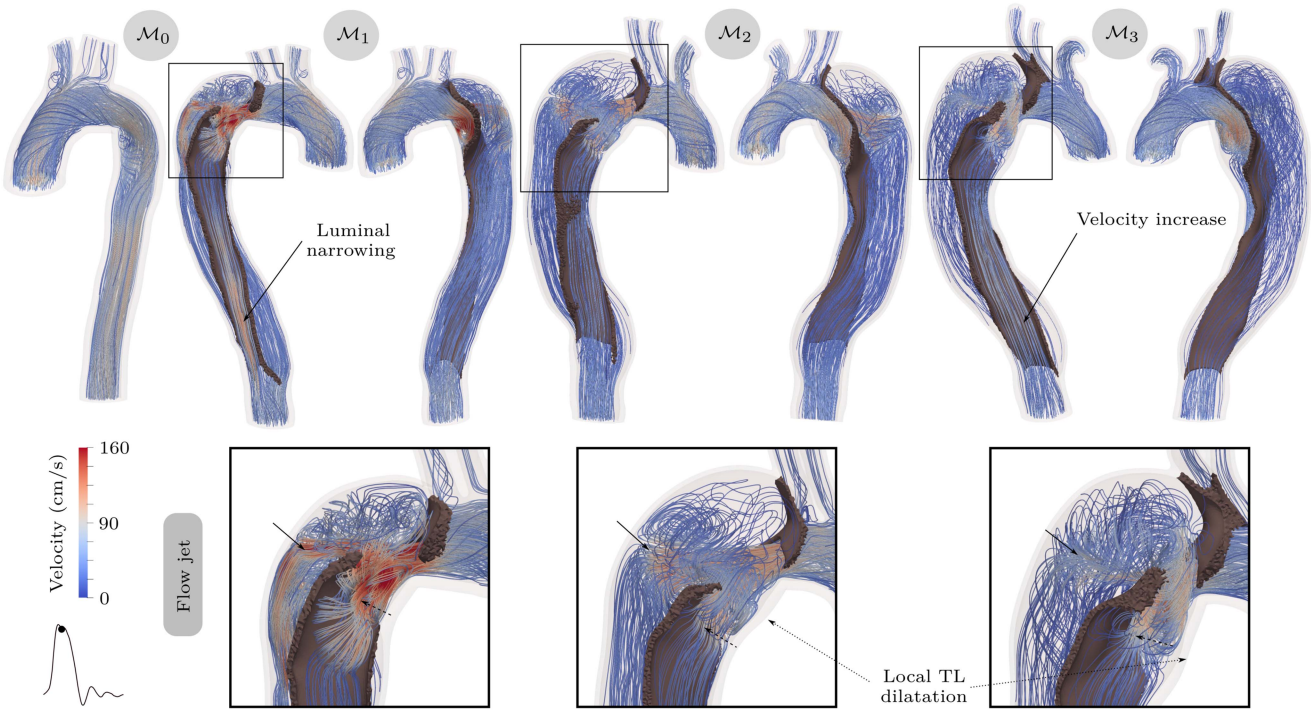

Fig. 4. Flow velocity for all models is displayed at peak systole, emphasizing the flow jet and the increase in blood velocity in the distal part of the FL. Additionally, a close-up view of the region where the flow jet impinges on the outer wall of the FL (solid arrow) is provided. This view also emphasizes a localized dilatation in the TL (dotted arrow) and the flow separation occurring in the TL (dashed arrow).

Growth over time: In the initial time interval between $\mathcal{M}_1$ and $\mathcal{M}_2$, we observed relatively uniform growth along the length of the aorta. In the TL, the median growth rate was 44 mm^2/year (ranging from 34 to 57 mm^2/year) measured at cross-sectional locations P3 to P13. A growth rate of 110 mm^2/year (ranging from 62 to 188 mm^2/year) was observed for the FL.

In the subsequent time interval between $\mathcal{M}_2$ and $\mathcal{M}_3$, the growth rate of the TL in the proximal section of the dissection (P3 to P5) was substantially higher and exceeded the growth rate 89 mm^2/year. However, it was slower in the mid to distal regions (P7 to P12), with rates below 13 mm^2/year. The FL growth rates during this interval were 54 mm^2/year (ranging from -61 to 84 mm^2/year). Similar to TL, the proximal part of FL grew the fastest, while the distal part of FL had negative growth rates, indicating shrinkage beyond P11. The temporal growth for both time intervals as well as for TL and FL is also visualized in the Supplementary Materials (Fig. S.1).

B. Flow Jet and Pattern

To examine the evolution of flow fields from the pre-dissection phase to the subacute and chronic phases, we visualized streamlines and velocity magnitudes at peak systole, as shown in Fig. 4 and videos in the Supplementary Materials. In $\mathcal{M}_0$, early systole shows predominantly laminar flow with vortical flow structures at peak systole near the downward bend distal to the aortic arch. The vortices extend across the aorta and result in corkscrew-shaped flow patterns that continue into diastole. In all models, the entry tear in the proximal descending aorta and the dissection flap post-dissection contribute to complex flow patterns throughout the cardiac cycle. Flow simulations indicate helical and vortical flow near the entry tear region and recirculation zones distal to it. During systole, a flow jet impinges on the FL surface through the entry tear, resulting in secondary flow patterns that propagate across the FL. The TL flow is mainly characterized by a recirculation zone distal to the entry tear, which returns to laminar flow in diastole. The FL flow jet velocity was highest in $\mathcal{M}_1$ with 185 cm/s, decreasing to 123 and 133 cm/s in $\mathcal{M}_2$ and $\mathcal{M}_3$, respectively.

Intriguingly, close-up views in Fig. 4 show subtle directional shifts of the flow jet, corresponding to the remodeling of the aortic geometry, affecting various regions on the outer wall of the FL over time (solid arrow). Furthermore, vector visualization of the velocity field highlights an impingement zone in the proximal TL, located distal to the entry tear in $\mathcal{M}_1$ and $\mathcal{M}_3$ (dashed arrow). This impingement zone on the TL surface appears to be a result of the recirculation of the velocity field in combination with the helical shape of the TL distal to the entry tear (dashed arrow; videos in the Supplementary Materials).

Impingement zone: A local pressure peak where the flow jet hits the outer wall of the FL is most pronounced in $\mathcal{M}_1$ with a pressure difference of about 11 mmHg. This peak decreases and changes position in $\mathcal{M}_2$ and $\mathcal{M}_3$ with a local pressure difference of 2 mmHg due to the remodeled aortic geometry. Fig. 5(b) illustrates the local pressure distribution in both lumina at peak systole across all models. Visualization of streamlines highlights another potentially relevant flow feature near the

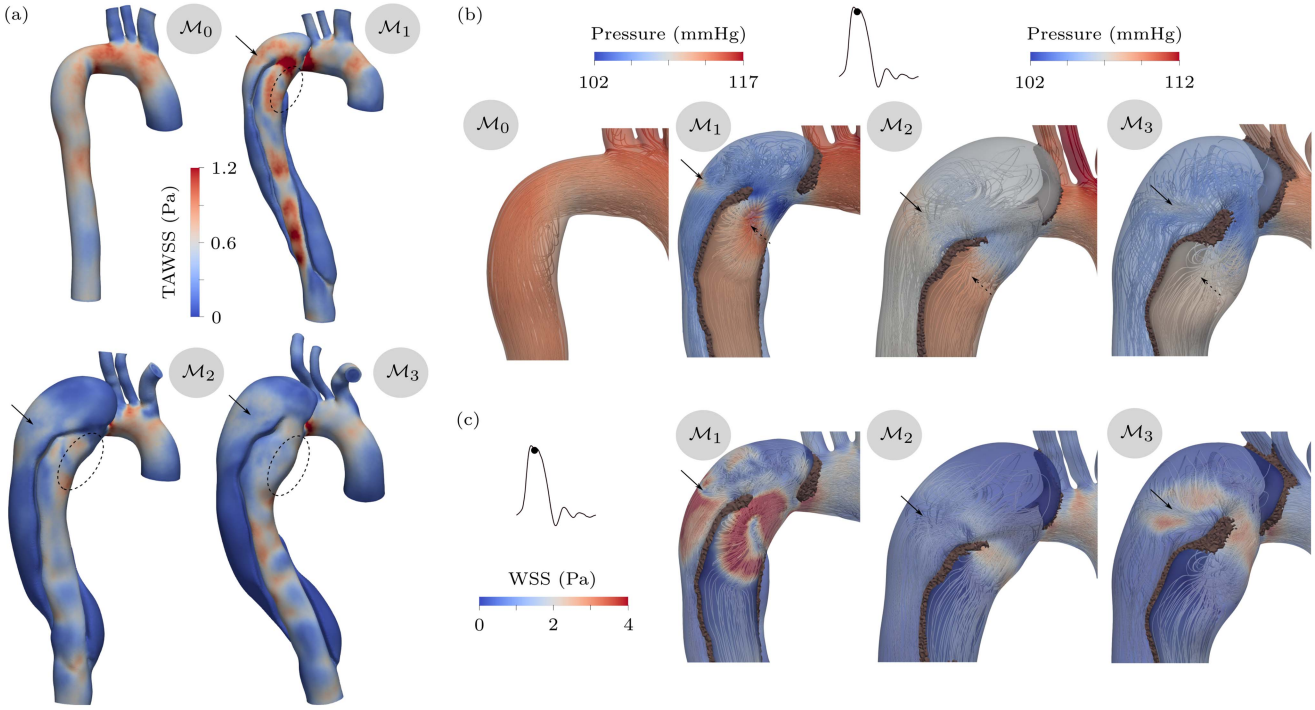

Fig. 5. TAWSS for all models is presented in (a) along with the local pressure distribution for all models in (b) and the local WSS for all post-dissection models in (c) within the proximal descending aorta at the peak systole. These illustrations highlight (a) the region of local dilatation in the TL (dashed circle) and FL (solid arrow), and (b) and (c) where the flow jet impinges the outer wall of the FL (solid arrow) and the TL (dashed arrow).

impingement zone: after impingement, flow is redirected tangentially to the aortic wall. In this region of tangential flow, we observe an increase in local wall shear stress (WSS) about 4 Pa or 40 dynes/cm^2 higher, as shown in Fig 5(c). Areas of increased WSS surround the zones of increased pressure, resulting in a distinct pattern of hemodynamic metrics near the entry tear (videos in the Supplementary Materials).

True lumen flow rate: The TL flow rate is defined as the ratio of the mean flow in the TL, averaged over the cardiac cycle, to the total flow, denoted as $F_{\mathrm{TL}} := Q_{\mathrm{TL}}/(Q_{\mathrm{TL}} + Q_{\mathrm{FL}})$. There is a substantial increase in the TL flow ratio from $\mathcal{M}_1$ to $\mathcal{M}_2$ to $\mathcal{M}_3$, with corresponding values of 18.3, 45.8, and 64.5%, respectively.

Velocity Field: To characterize the velocity field in TL and FL, we calculated the average flow velocity across the cross-section at peak systole ($T = 0.225$ s with a cycle length of 1 s). The velocity within the FL shows minimal variation in all follow-up models. Specifically, the mean FL velocity in $\mathcal{M}_1$ was recorded at 264 cm/s, in $\mathcal{M}_2$ at 141 cm/s, and in $\mathcal{M}_3$ at 94 cm/s. Conversely, in the TL, flow velocities increased toward the middle and distal segments of the dissected aorta in $\mathcal{M}_1$ (616 cm/s at P11) and $\mathcal{M}_3$ (423 cm/s at P10). For the position and numbering of the segments, the reader is referred to Fig. 3. In contrast, flow simulations for $\mathcal{M}_2$ showed the highest TL velocity at the proximal end with 395 cm/s, while velocities did not exceed 270 cm/s in the distal regions.

Reversed flow: The reverse flow fraction quantifies the extent of retrograde flow relative to net flow throughout the cardiac cycle. We assessed the TL-reverse flow fraction $\mathrm{RF}_{\mathrm{TL}}$ and the FL-reverse flow fraction $\mathrm{RF}_{\mathrm{FL}}$ at cross-section P3. For $\mathcal{M}_1$, $\mathcal{M}_2$, and $\mathcal{M}_3$, the values of $\mathrm{RF}_{\mathrm{TL}}$ were recorded as $\{1.67, 0.37, 0.55\}$, and those of $\mathrm{RF}_{\mathrm{FL}}$ as $\{0.22, 0.85, 0.75\}$, respectively.

Time-averaged wall shear stress: Time-averaged wall shear stress (TAWSS) represents the temporal average of the WSS over the cardiac cycle. Elevated TAWSS values are found in the proximal descending aorta and the FL of $\mathcal{M}_1$, characterized by a narrow FL diameter and a strong flow jet. In $\mathcal{M}_1$, the TL has the highest TAWSS values, especially around the entry tear and in the distal TL, which correlates with a tapered cross-sectional area and increased flow velocities, see Fig. 5(a). As the disease progresses and the TL expands, the TAWSS values in the TL generally decrease in $\mathcal{M}_2$ and then display a slight increase in TAWSS in $\mathcal{M}_3$. This is accompanied by an increase in average velocity distal of P6, as depicted in Fig. 4.

C. Luminal Pressure and Flap Displacement

In a healthy aorta, pressure typically decreases gradually along its length. However, in aortic dissections, this pressure drop can be more intricate [12]: (i) sharp pressure drops are particularly noticeable at regions with cross-sectional narrowing, such as the entry or exit tear. (ii) The taper of the cross-sectional area, seen here in the TL, contributes to an increased pressure reduction. Overall, these dynamics are influenced by TL and FL outflow and capacitance as well as outflow resistance.

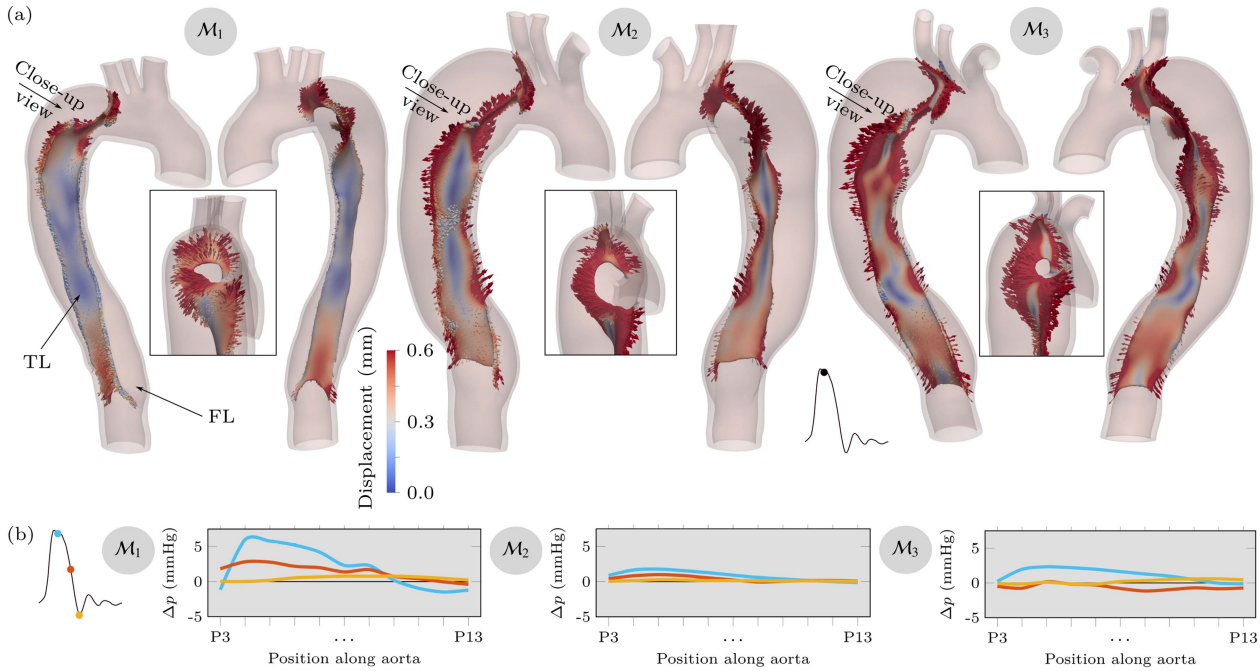

Fig. 6. (a) Displacement magnitude and direction of the displacement of the dissection flap at peak systole are shown in all models; TL and FL highlighted for enhanced visualization. (b) Corresponding TL-to-FL pressure difference Δp at 14 positions along the aorta (P1 to P14) is depicted for all models at three cardiac cycle phases (peak systole: cyan, mid-deceleration systole: orange, and end systole: yellow; see scale).

Aortic pressure: We report the pressure at predefined locations (P3 to P13) at three selected time points: peak systole ($T = 0.225$ s), mid-deceleration systole ($T = 0.39$ s), and end systole ($T = 0.50$ s), shown in Fig. 3 and in the Supplementary Materials (Table S.V). In the ascending aorta (P1), the pressure declined rapidly from peak systole to end systole with a difference of the 16 and 18 mmHg, in $\mathcal{M}_0$ and $\mathcal{M}_1$, respectively. During the chronic phase ($\mathcal{M}_2$ and $\mathcal{M}_3$) this pressure difference was reduced to 6 and 4 mmHg, respectively, caused by a reduction of peak systolic and an increase of end-diastolic pressure, see Supplementary Materials (Table S.V). These observations correspond to a slower fall in blood pressure and an increased pressure load during diastole. A notable increase was observed in the distal FL (P9 to P13) in $\mathcal{M}_3$, where pressures at the end systole surpassed those at the peak systole (dotted circle). Consequently, the FL experienced a higher diastolic pressure load in the chronic stage of the disease.

Additionally, we calculated the mean pressure over the cardiac cycle at each aortic site, as shown in the Supplementary Materials (Table S.V). Before dissection, mean aortic pressure varied by 0.4 mmHg along the descending aorta. Within the FL, the cycle-averaged pressure varied by less than 0.1 mmHg at T_1, T_2, and T_3. In contrast, the TL displayed greater mean pressure variability (1.4 mmHg) in the subacute phase, possibly due to its increased taper, as detailed in Table II. At T_2, and T_3, this pressure variability in the TL reduced to pre-dissection levels, see Supplementary Materials (Table S.V).

Interluminal pressure difference: We defined the pressure difference as $\Delta p := p_{\mathrm{TL}} - p_{\mathrm{FL}}$, where p_{TL} and p_{FL} represent the mean pressure in the TL and FL, respectively, while Δp along with material stiffness is considered a key driver of the motion of the dissection flap. The maximum pressure difference is typically seen in the proximal aorta, as depicted in Fig. 6(b). For $\mathcal{M}_1$ the largest pressure difference was $\Delta p = 7.0$ mmHg at $T = 0.29$ s at P5. In $\mathcal{M}_2$ the pressure difference peaked at 2.3 mmHg at $T = 0.26$ s at P4, and in $\mathcal{M}_3$ it reached 3.5 mmHg at $T = 0.20$ s at P5. During diastole, the pressure difference in $\mathcal{M}_1$ remained below 1.0 mmHg, in $\mathcal{M}_2$ below 0.3 mmHg and in $\mathcal{M}_3$ below 0.6 mmHg.

Negative pressure differences, where the FL pressure exceeds the TL pressure, typically occurred in the mid to distal dissected aorta (P8 in $\mathcal{M}_1$, P9 in $\mathcal{M}_2$, and P12 in $\mathcal{M}_3$), with minimum values of -1.9 mmHg in $\mathcal{M}_1$, -0.54 mmHg in $\mathcal{M}_2$, and -1.7 mmHg in $\mathcal{M}_3$. In both $\mathcal{M}_1$ and $\mathcal{M}_2$ the minimum was observed at early diastole ($T = 0.43$ s), while in $\mathcal{M}_3$ it was at $T = 0.28$ s or mid-deceleration systole.

Flap displacement: Fig. 6(a) shows the displacement of the dissection flap at the peak systole, corresponding to the pressure differences illustrated in Fig. 6(b). The overall displacements are modest and do not exceed 0.6, 1.6, 1.6, and 1.8 mm in $\mathcal{M}_0$, $\mathcal{M}_1$, $\mathcal{M}_2$, and $\mathcal{M}_3$, respectively. Before dissection, the largest displacement was observed in the outer wall of the BCT. After dissection, the largest displacements occurred in the flap, where the predominant direction of displacement is in-plane. In early systole ($T = 0.18$ to 0.2 s) the dissection flap at the middle of the entry tear opening is stretched towards the FL, while the distal flap regions tend to move towards the TL, as shown in Fig. 6(a). Later in the cardiac cycle ($T = 0.34$ to 0.38 s), the greatest in-plane dilatation of the flap is observed, coinciding with the overall dilatation of the proximal aorta. In fact, the flap displacement changes qualitatively with increased elasticity. In additional simulations with reduced flap stiffness, the flap

motion shifted predominantly to the cross-plane direction, see Section II-C in the Supplementary Materials.

IV. Discussion

In this longitudinal study, we investigated a patient with type B aortic dissection, focusing on the evolution of the disease over multiple follow-up imaging sessions using FSI simulations. Our main interest was the correlation of flow properties, hemodynamic markers and aortic remodeling, a challenging task due to the complex remodeling processes in aortic dissection. As is often observed in aortic dissections, this patient experienced continuous growth in maximum aortic diameter, TL and FL volumes, and cross-sectional areas. When studying aortic remodeling, we noted a decrease in the initial high tapering ratio (3.4) of the TL, while the initial low tapering ratio of the FL (1.2) increased as the disease progressed. Characteristically, the region of greatest growth was located directly distal to the LSA in the entry tear area in the proximal descending aorta.

The entry tear area is distinguished by a flow jet penetrating the FL through the entry tear and creating an impingement zone on the structurally compromised outer wall of the FL, which is characterized by locally increased pressure and WSS. This phenomenon is a hallmark of aortic dissection [12]. During systole, blood flows at high velocity through the entry tear into the FL and hits the outer wall. The peak velocity of this flow jet occurred in the subacute phase, marked by a relatively small aortic diameter and the greatest local pressure increase in the impingement zone of the FL. In the chronic disease stage, the magnitude of the flow jet was smaller, which may be caused by a larger size of the entry tear in the models $\mathcal{M}_2$ and $\mathcal{M}_3$, although the orientation of the entry tear in the flow field possibly played also a role. The simultaneously observed increased FL diameter in these models further reduced the effect of the later impingement of the flow jet on the FL surface. Notably, during this first time interval, the proximal FL exhibits the highest growth rate, suggesting that the influence of the flow jet may contribute to aortic remodeling. A detailed investigation of streamlines, pressure, and WSS revealed a complex interaction between flow impingement and increased local pressure surrounded by tangential flow with elevated WSS. The exact location of the impingement zone varies throughout the cardiac cycle and longitudinally over disease progression, creating a region of substantial hemodynamic changes compared to the pre-dissection state. The decreased flow jet velocity in $\mathcal{M}_2$ and $\mathcal{M}_3$ is accompanied by a reduction in pressure and WSS elevation in the impingement zone and, interestingly, by a reduced FL growth rate in the proximal dissection.

We hypothesize that the local hemodynamic changes in the impingement zone described above are the driving force behind local morphological changes by aortic growth and remodeling. This hypothesis is even more interesting because an impingement zone on the TL surface, identified in $\mathcal{M}_3$, coincides with the area of strongest TL growth (Fig. S.1 and videos in the Supplementary Materials). In summary, the region affected by the flow jet correlates with locally increased pressure and WSS, which likely play a role in aortic remodeling.

While medial degeneration in aortic dissections, including accumulation of glycosaminoglycan and fragmentation of elastic fibers, is well understood [18], [37], understanding of remodeling in the new layers remains limited. The remodeling probably differs between the TL with its intact endothelial layer and delaminated structures such as the dissection flap and the FL outer wall [4]. Delamination permits monocytes and leukocytes to penetrate the wall, triggering neointima formation and inflammation. Current studies suggest that inflammation is predominantly acute and transient [38], with the development of a neointima leading to thickening of the dissected layers within days to weeks [39]. Additionally, altered WSS can affect wall microstructure, as endothelial cells respond to these changes and aim to restore homeostasis [40], [41], [42].

The influence of TL and FL pressure on growth and remodeling is shown in Figs. 3 and 6. The TL-to-FL pressure difference is typically less than 6 mmHg [4]. Computational and clincal studies suggest that FL pressurization promotes aortic dilatation [5], [6], probably due to hypertensive remodeling, as the thinner outer FL wall is exposed to similar pressures as the thicker TL wall in the acute and subacute phases. Aortic hypertension normalizes increased wall stress through collagen accumulation, smooth muscle growth, and proteoglycan deposition, leading to structural stiffening and thickening of the outer FL wall and a dissection flap during the chronic phase [39], although the effects vary and depend on the injury response and changes in the microstructure. Recent computational studies confirm these findings [38], [43].

In addition to local variations in the entry tear region, we investigated changes in blood pressure and TAWSS along the aorta. In all models, post-dissection blood pressure was homogeneous along the length of the FL and its value agreed well with the distal TL blood pressure, indicating that the patient's exit tear was large enough to avoid a pressure build-up in the FL. Conversely, the TL blood pressure in all models showed a gradual decrease along the length of the aorta, similar to the pressure decrease along the aorta in the model before dissection. This pressure loss was measured at 0.4 to 0.6 mmHg in $\mathcal{M}_0$, $\mathcal{M}_2$, and $\mathcal{M}_3$, but it showed a substantial increase to 1.6 mmHg in the subacute phase ($\mathcal{M}_1$). At the same time, in $\mathcal{M}_1$, the TL mean blood pressure was substantially lower compared to its state before dissection ($\mathcal{M}_0$), and, interestingly, also the values in $\mathcal{M}_2$ and $\mathcal{M}_3$.

These observations highlight the hemodynamic deviation of the subacute phase compared to the pre-dissection state and, interestingly, also to the chronic stages of the disease. In $\mathcal{M}_1$, we observed (i) the fastest flow jet through the entry tear with substantially increased pressure and WSS in the impingement region, (ii) the largest TAWSS over the entire length of the TL, and (iii) a substantially increased pressure drop along the TL and an overall reduced mean blood pressure in the dissected region of the aorta.

Subsequent morphological remodeling appears to modulate these deviations from the original hemodynamic state via: (i) a reduction in TL tapering, (ii) an increase in FL diameter at the entry tear, effectively reducing the local variations in pressure, and WSS (iii) an increase in aortic and TL diameter near the

entry tear region, reducing the pressure drop from the aortic arch into the TL and the effects of the flow jet impingement on the TL wall. Further investigations are essential to thoroughly understand the local influence of various hemodynamic features on the remodeling process and to further investigate remodeling in the chronic stage of the disease [44].

V. Limitations

In silico FSI simulations derived from patient-specific data in clinical settings encounter several obstacles: first, the material parameters for external tissue support and the mechanical tissue characteristics, including wall thickness and fiber orientations often rely on assumptions from the literature rather than on patient-specific data. This is due to the lack of detailed, layer-specific longitudinal data on the mechanical properties of dissected tissues (particularly since the presented patient was diagnosed with Marfan disease), which led us to select representative material parameters and wall thicknesses. While clinical data indicate remodeling and stiffening of the dissection flap from acute and subacute to chronic disease stages [39], detailed data of this nature were not available. To gain insight into the effect of flap stiffness in the subacute phase, we have provided additional simulations in Section II-C in the Supplementary Materials. A substantial challenge arises from the inability to accurately measure wall thickness using CTA scans. This parameter is typically region-specific and may change over time. Likewise, modeling external tissue support with widely accepted parameters raises questions regarding its exact correspondence to *in vivo* conditions. Additionally, computing fiber directions in aortic dissections presents challenges, particularly in the tear region and at the transition between the dissection flap and the aortic wall.

Second, flow boundary conditions such as inlet flow rate and flow splits were sourced from *in vitro* measurements (MRI) and were not obtained as part of routine clinical practice. Patient-specific blood pressure data were not available for all imaging appointments, resulting in available data being used for all simulations. Although these assumptions result in deviations from the *in vivo* setting, they also simplify longitudinal comparison by allowing identical boundary conditions to be specified for all models. Despite the potential effects that these assumptions might have on the simulations results, we believe that they did have a significant impact on the overall analysis and results presented.

The third limitation concerns the prestress algorithm. While prestressing the solid domain is often used in FSI simulations for realistic initial deformation, it presents problems: (i) using a prestress tensor instead of determining the actual stress-free geometry results in zero strain at diastole. This contradicts the stress-strain curve of the material model because the material model is based on a stress-strain curve that assumes a true stress-free geometry for the zero-strain data point, resulting in an inaccurate assessment of the material response and increasing the uncertainty of the volume area response. Unfortunately, switching to the prestressing algorithm that identifies a stress-free geometry brings its own limitations, as there is evidence that such configurations are often ambiguous or may not exist at all [28]. (ii) Likewise, the prestress tensor itself is not unique, although the algorithm provides a specific solution [28]. It remains uncertain how accurately this tensor reflects the actual stress state of the aortic wall at diastole. Further discussion can be found in the study by Schussnig et al. [15]. The significance of stress results is further reduced by the ongoing growth and remodeling of blood vessels, which impact the absolute stresses of the aortic tissue *in vivo*. Therefore, we did not include stress results at this stage.

Although this study focuses on a single patient, the inclusion of multiple follow-ups in FSI simulations of a patient-specific aortic dissection remains unique [4], primarily due to the significant computational effort. However, expanding the number of patients is essential for more robust and generalizable conclusions.

VI. Conclusion and Future Work

This study represents the first longitudinal analysis of a patient-specific aortic dissection, which uniquely incorporates the anisotropic behavior of the aortic wall and the layer-specific thickness of newly formed tissue layers. The findings highlight the interplay between altered hemodynamics and aortic remodeling, particularly in relation to changes in wall microstructure and their impact on TL and FL dilatation during disease progression.

We observed the greatest hemodynamic variation during the subacute phase, followed by a return of certain parameters to pre-dissection values. Notably, flow jet velocity at the entry tear decreased as disease progressed, leading to locally increased WSS and blood pressure in the FL impingement zone, which correlated with significant aortic dilatation. Similar effects were observed for the TL post-entry tear. Comparable pressure levels in TL and FL suggest a hypertensive-like state in FL, especially in acute phases with thinner outer wall. These changes in WSS, pressure and hypertension are known to be related to alterations in mechanosensing within the aortic wall.

The patient case evaluated serves as a pivotal example for future research. First, computational methods could be implemented for realistic, physiological evaluation of *in vivo* stresses in blood vessels. Second, a growth and remodeling framework for patient-specific aortic dissections could be developed using available longitudinal data, such as those provided by [44]. Third, the influence of rigid Dacron grafts (or other types) on output metrics can be analyzed, particularly when compared to pre- and post-dissection follow-ups. Finally, the application of advanced registration algorithms would enable statistical evaluation of surface metrics (pressure, WSS, oscillatory shear index, etc.) for local growth and provide insights into graft deployment and aortic dilatation in patients with aortic dissection.

Data accessibility

The data from this study are openly available in the Vascular Model Repository at https://vascular model.com. The SimVascular software with svFSI is available at https://simvascular.github.io.

REFERENCES

[1] D. Fleischmann et al., "Imaging and surveillance of chronic aortic dissection: A scientific statement from the American Heart Association," *Circulation: Cardiovasc. Imag.*, vol. 15, no. 3, 2022, Art. no. e000075.

[2] A. Evangelista et al., "Insights from the international registry of acute aortic dissection: A 20-year experience of collaborative clinical research," *Circulation*, vol. 137, no. 17, pp. 1846–1860, 2018.

[3] J. L. Tolenaar et al., "Morphologic predictors of aortic dilatation in type B aortic dissection," *J. Vasc. Surg.*, vol. 58, no. 5, pp. 1220–1225, 2013.

[4] M. Rolf-Pissarczyk et al., "Mechanisms of aortic dissection: From pathological changes to experimental and in silico models," *Prog. Mater. Sci.*, vol. 150, 2025, Art. no. 01363.

[5] D. Marlevi et al., "False lumen pressure estimation in type B aortic dissection using 4D flow cardiovascular magnetic resonance : Comparisons with aortic growth," *J. Cardiovasc. Magn. Reson.*, vol. 23, 2021, Art. no. 51.

[6] H. Xu et al., "Computed tomography-based hemodynamic index for aortic dissection," *J. Thoracic Cardiovasc. Surg.*, vol. 162, no. 2, pp. e165–e176, 2021.

[7] R. E. Clough et al., "A new imaging method for assessment of aortic dissection using four-dimensional phase contrast magnetic resonance imaging," *J. Vasc. Surg.*, vol. 55, no. 4, pp. 914–923, 2012.

[8] C. Stokes et al., "The influence of minor aortic branches in patient-specific flow simulations of type-B aortic dissection," *Ann. Biomed. Eng.*, vol. 51, no. 7, pp. 1627–1644, 2023.

[9] C. Menichini et al., "A computational model for false lumen thrombosis in type B aortic dissection following thoracic endovascular repair," *J. Biomech.*, vol. 66, pp. 36–43, 2017.

[10] A. Jafarinia et al., "Morphological parameters affecting false lumen thrombosis following type B aortic dissection: A systematic study based on simulations of idealized models," *Biomech. Model Mechanobiol.*, vol. 22, pp. 885–904, 2023.

[11] K. Bäumler et al., "Fluid–structure interaction simulations of patient-specific aortic dissection," *Biomech. Model Mechanobiol.*, vol. 19, pp. 1607–1628, 2020.

[12] J. Zimmermann et al., "Hemodynamic effects of tear size in aortic dissections: Comparing in vitro flow magnetic resonance imaging with fluid–structure interaction simulations," *Sci. Rep.*, vol. 13, 2023, Art. no. 22557.

[13] Y. Zhu et al., "Fluid–structure interaction simulations of repaired type A aortic dissection: A comprehensive comparison with rigid wall models," *Front. Physiol.*, vol. 13, 2022, Art. no. 913457.

[14] X. Wang et al., "Fluid–structure interaction study for biomechanics and risk factors in Stanford type A aortic dissection," *Int. J. Numer. Method Biomed. Eng.*, vol. 39, 2023, Art. no. e3736.

[15] R. Schussnig et al., "On the role of tissue mechanics in fluid–structure interaction simulation of patient-specific aortic dissection," *Int. J. Numer. Methods Eng.*, vol. 125, 2024, Art. no. e7478.

[16] R. Schussnig et al., "Semi-implicit fluid–structure interaction in biomedical applications," *Comput. Methods Appl. Mech. Eng.*, vol. 400, 2022, Art. no. 115489.

[17] G. A. Holzapfel, T. C. Gasser, and R. W. Ogden, "A new constitutive framework for arterial wall mechanics and a comparative study of material models," *J. Elasticity Phys. Sci. Solids*, vol. 61, pp. 1–48, 2000.

[18] M. K. Halushka et al., "Consensus statement on surgical pathology of the aorta from the Society for Cardiovascular Pathology and the Association for European Cardiovascular Pathology: II. Noninflammatory degenerative diseases - nomenclature and diagnostic criteria," *Cardiovasc. Pathol.*, vol. 25, no. 3, pp. 247–257, 2016.

[19] G. Mistelbauer et al., "Visualization of aortic diameter changes over time in an aortic surveillance program," in *Proc. ECR Book Abstracts–C. – Sci. Educ. Exhibits*, 2017, pp. C–1905.

[20] A. Updegrove et al., "SimVascular: An open source pipeline for cardiovascular simulation," *Ann. Biomed. Eng.*, vol. 45, pp. 525–541, 2016.

[21] H. Si, "Adaptive tetrahedral mesh generation by constrained Delaunay refinement," *Int. J. Numer. Methods Eng.*, vol. 75, no. 7, pp. 856–880, 2008.

[22] M. Amabili et al., "Biomechanical characterization of a chronic type A dissected human aorta," *J. Biomech.*, vol. 110, 2020, Art. no. 109978.

[23] W. N. W. A. Naim et al., "A perspective review on numerical simulations of hemodynamics in aortic dissection," *Sci. World J.*, vol. 2014, 2014, Art. no. 652520.

[24] T. C. Gasser, R. W. Ogden, and G. A. Holzapfel, "Hyperelastic modelling of arterial layers with distributed collagen fibre orientations," *J. Roy. Soc. Interface*, vol. 3, no. 6, pp. 15–35, 2006.

[25] M. Rolf-Pissarczyk et al., "A discrete approach for modeling degraded elastic fibers in aortic dissection," *Comput. Methods Appl. Mech. Eng.*, vol. 373, 2021, Art. no. 113511.

[26] A. J. Schriefl et al., "Determination of the layer-specific distributed collagen fibre orientations in human thoracic and abdominal aortas and common iliac arteries," *J. Roy. Soc. Interface*, vol. 9, no. 71, pp. 1275–1286, 2012.

[27] M. Rolf-Pissarczyk et al., "Efficient computational modelling of smooth muscle orientation and function in the aorta," *Proc. Roy. Soc. A*, vol. 477, 2021, Art. no. 20210592.

[28] M.-C. Hsu and Y. Bazilevs, "Blood vessel tissue prestress modeling for vascular fluid–structure interaction simulation," *Finite Elements Anal. Des.*, vol. 47, no. 6, pp. 593–599, 2011.

[29] P. Moireau et al., "External tissue support and fluid–structure simulation in blood flows," *Biomech. Model Mechanobiol.*, vol. 11, no. 1/2, pp. 1–18, 2012.

[30] P. Reymond et al., "Physiological simulation of blood flow in the aorta: Comparison of hemodynamic indices as predicted by 3-D, FSI, 3-D rigid wall and 1-D models," *Med. Eng. Phys.*, vol. 35, no. 6, pp. 784–791, 2013.

[31] I. E. Vignon-Clementel et al., "Outflow boundary conditions for three-dimensional finite element modeling of blood flow and pressure in arteries," *Comput. Methods Appl. Mech. Eng.*, vol. 195, no. 29–32, pp. 3776–3796, 2006.

[32] C. Zhu et al., "svFSI: A multiphysics package for integrated cardiac modeling," *J. Open Source Softw.*, vol. 7, no. 78, 2022, Art. no. 4118.

[33] A. L. Marsden and M. Esmaily-Moghadam, "Multiscale modeling of cardiovascular flows for clinical decision support," *Appl. Mech. Rev.*, vol. 67, no. 3, 2015, Art. no. 030804.

[34] J. Seo, D. E. Schiavazzi, and A. L. Marsden, "Performance of preconditioned iterative linear solvers for cardiovascular simulations in rigid and deformable vessels," *Comput. Mech.*, vol. 64, pp. 717–739, 2019.

[35] M. Esmaily-Moghadam, Y. Bazilevs, and A. L. Marsden, "A bi-partitioned iterative algorithm for solving linear systems arising from incompressible flow problems," *Comput. Methods Appl. Mech. Eng.*, vol. 286, pp. 40–62, 2015.

[36] M. R. Pfaller et al., "On the periodicity of cardiovascular fluid dynamics simulations," *Ann. Biomed. Eng.*, vol. 49, pp. 3574–3592, 2021.

[37] J. D. Humphrey, "Possible mechanical roles of glycosaminoglycans in thoracic aortic dissection and associations with dysregulated transforming growth factor-β," *J. Vasc. Res.*, vol. 50, no. 3, pp. 198–9, 2013.

[38] L. Gheysen et al., "Growth and remodeling of the dissected membrane in an idealized dissected aorta model," *Biomech. Model Mechanobiol.*, vol. 23, pp. 413–431, 2023.

[39] S. Peterss et al., "Changing pathology of the thoracic aorta from acute to chronic dissection: Literature review and insights," *J. Amer. College Cardiol.*, vol. 68, no. 10, pp. 1054–65, 2016.

[40] J. D. Humphrey, E. Dufresne, and M. A. Schwartz, "Mechanotransduction and extracellular matrix homeostasis," *Nat. Rev. Mol. Cell Biol.*, vol. 15, no. 12, pp. 802–12, 2014.

[41] D. G. Guzzardi et al., "Valve-related hemodynamics mediate human bicuspid aortopathy: Insights from wall shear stress mapping," *J. Amer. Coll Cardiol.*, vol. 66, no. 8, pp. 892–900, 2015.

[42] M. Y. Salmasi et al., "High wall shear stress can predict wall degradation in ascending aortic aneurysms: An integrated biomechanics study," *Front. Bioeng. Biotechnol.*, vol. 9, 2021, Art. no. 750656.

[43] S. Zhang et al., "Patient-specific finite element modeling of aneurysmal dilatation after chronic type B aortic dissection," in *Computational Biomechanics for Medicine: Towards Translation and Better Patient Outcomes*, P. M. F. Nielsen et al., Eds. Berlin, Germany: Springer, 2022, pp. 15–38.

[44] E. L. Schwarz et al., "A fluid–solid-growth solver for cardiovascular modeling," *Comput. Methods Appl. Mech. Eng.*, 2023, Art. no. 116312.